

**Paper 0**

**J. van Irsel<sup>1</sup>, K. A. Lynch<sup>1</sup>, A. C. Mule<sup>1</sup>, M. Zettergren<sup>2</sup>**

<sup>1</sup>Department of Physics and Astronomy, Dartmouth College, Hanover, NH, 03755 USA

<sup>2</sup>Physical Sciences Department, Embry-Riddle Aeronautical University, Daytona Beach, FL, 32114 USA

**Key Points:**

- enter point 1 here
- enter point 2 here
- enter point 3 here

9      **Abstract**

10     Enter your Abstract here

11     **Plain Language Summary**

12     Enter your Plain Language Summary here or delete this section.

13     **1 Introduction**

14     **1.1 Motivation**

15     **What does this paper provide and why?** Measurements of auroral arc systems are  
 16 often sparse, heterogeneous, and largely distributed, yet ionospheric models generally re-  
 17 quire continuous 2D input drivers. Moreover, the distribution is commonly no more than  
 18 one, maybe two sets of dense across-arc data tracks leaving little to no information on  
 19 along-arc morphologies. Luckily, information about these morphologies is something that  
 20 all-sky imagery can provide.

21     This paper outlines three empirical methods for creating electrostatic, continuous,  
 22 2D, topside F-region convection boundary conditions from distributed optical data pro-  
 23 vided by all-sky, multi-spectral imagery and plasma flow data tracks provided by space-  
 24 craft, sounding rockets and/or radar measurements. These methodologies focus on typ-  
 25 ical sheet-like discrete auroral arc structures with high across- to along-arc gradient ra-  
 26 tios. Furthermore, this paper looks at the use of these boundary conditions in driving  
 27 and assessing 3D auroral ionospheric simulations.

28     **Why do we care about 3D auroral ionospheric simulations?** The understanding of  
 29 auroral arc scale science plays an important role in interpreting magnetosphere-ionosphere  
 30 (MI) coupling, the ionospheric end of which itself involves complex, system level science  
 31 which is ongoing (Wolf, 1975; Seyler, 1990; Cowley, 2000; Lotko, 2004; Fujii et al., 2011,  
 32 2012; Marghitu, 2012; Khazanov et al., 2018; Clayton et al., 2019, 2021; Yano & Ebihara,  
 33 2021; Lynch et al., 2022; Enengl et al., 2023; Wang et al., 2024). MI coupling de-  
 34 demands self-consistent, topside maps of field-aligned current (FAC) and convection plasma  
 35 flow that agree with a 3D ionospheric conductivity volume created by charged particle,  
 36 auroral precipitation. This is why the auroral ionosphere plays a non-passive role in this  
 37 coupling. At high latitudes, the 2D topside relation between quasi-static convective flow,  
 38 FAC, and conductances is (Kelley, 2009, Eq. 8.15):

$$j_{\parallel}(x, y) = \Sigma_P \nabla_{\perp} \cdot \mathbf{E} + \mathbf{E} \cdot \nabla_{\perp} \Sigma_P + (\mathbf{E} \times \mathbf{b}) \cdot \nabla_{\perp} \Sigma_H, \quad (1)$$

39 where  $j_{\parallel}$  is the topside map of FAC orthogonal to the local magnetic field,  $\Sigma_{P,H}$  are the  
 40 height-integrated Pedersen and Hall conductivities, i.e. conductances,  $\mathbf{E}$  is the ionospheric  
 41 electric field, and  $\mathbf{b} = \mathbf{B}/B$  is the magnetic field direction. This explains, in the ab-  
 42 sence of strong dynamics, how magnetospheric currents and convection patterns couple  
 43 to the ionosphere given 2D conductance maps. However, this perspective ignores the re-  
 44 active effects of the ionosphere and, in fact, it integrates out all altitudinal depen-  
 45 dencies. E.g. finite, altitude dependent recombination times in combination with plasma trans-  
 46 port can produce complex 3D electron density structures providing an auroral precip-  
 47 itation hysteresis in conductance maps. Moreover, the 3D conductivity volume is highly  
 48 sensitive to auroral precipitation by means of impact ionization. In particular, the pre-  
 49 precipitation energy spectra determine ionization rate profiles that are altitude dependent  
 50 (Fang et al., 2008, 2010). This is why it is important to study the full 3D picture of au-  
 51 roral system science. This is done by looking at FAC closure influenced by auroral pre-  
 52 precipitation in a way that is both geophysical and self-consistent with plasma convection.  
 53 To do this, we need 3D ionospheric simulations which require continuous 2D input drivers.

54            **1.2 Background**

55            **Nicolls 2014 and Bristow 2016.** Nicolls et al. (2014) undertake the mapping (or “imaging”)  
 56            of 2D electric field distributions using line-of-sight (LOS) radar plasma flow mea-  
 57            surements. They outline a regularized least-squares fitting algorithm which takes direct  
 58            LOS flow measurements along with their measurement error and produces a 2D electric  
 59            potential map. This is a difficult feat in that a single LOS measurement only carries in-  
 60            formation on one component of the electric field; it requires multiple beams to discover  
 61            information about the full vector field. Part of their regularization minimizes the mean  
 62            squared curvature of the potential field (with a personal tailoring parameter) which re-  
 63            sults in the smoothest possible solutions and minimizes gradients isotropically, something  
 64            not well suited for sheet-like auroral arcs.

65            Bristow et al. (2016) approach the same problem differently using Local Divergence-  
 66            Free Fitting (LDFF). They impose the local constraint of divergence-free plasma con-  
 67            vection and treat this in the same way the recomposition of two LOS measurements con-  
 68            straint is treated. This achieves larger gradients, and in turn higher spatial resolution,  
 69            but this is still indiscriminate to along- or across-arc directions.

70            **Lompe, AMIE, and KRM.** Laundal et al. (2022) describe methodology for the Lo-  
 71            cal mapping of polar ionospheric electrodynamics (Lompe). This is an assimilative tool  
 72            that gathers relatively dense, heterogeneous observational data provided by ground/space  
 73            magnetometers, optical all-sky observatories, and radars, and performs a local/regional  
 74            mapping of the polar ionospheric electrodynamics. They point out that they use Spher-  
 75            ical Elementary Current Systems (SECS) (Amm, 1997) instead of the more global spher-  
 76            ical bases used by other assimilative tools like the Kamide-Richmond-Matsushita (KRM)  
 77            (Kamide et al., 1981) and the Assimilative Mapping of Ionospheric Electrodynamics (AMIE)  
 78            (Richmond & Kamide, 1988) methods, which allows more flexibility when it comes to  
 79            spatial scales.

80            **Clayton method.** This paper includes a formalization of techniques developed dur-  
 81            ing the phase A Concept Study Report (CSR) for the Auroral Reconstruction CubeSwarm  
 82            (ARCS) mission proposal (Lynch et al., 2024; Erlandson et al., 2024) as well as a con-  
 83            tinuation of techniques developed by Clayton et al. (2019, 2021) with several improve-  
 84            ments. We outline methodologies for the continuous mapping of plasma flow data tracks  
 85            which focus on auroral physical and gradient scale lengths, and discrete sheet-like mor-  
 86            phologies.

87            **1.3 Outline.**

88            Section 2 describes the reconstruction, replication, and weighted replication method-  
 89            ology along with an example usages of each one. Section 3 outlines and compares two  
 90            example 3D auroral multi-fluid simulations driven by plasma flow maps derived by the  
 91            replication method in Section 2.2. In section 4 we discuss our results and outline how  
 92            we intend to use these methods in future work and we conclude this work in Section 5.

93            **2 Methodologies**

94            We outline three methods for developing continuous plasma flow maps from lim-  
 95            ited remote sensed or in situ flow data tracks. Section 2.1 outlines the first methodol-  
 96            ogy coined “reconstruction”, which stems from science section in the ARCS CSR (Lynch  
 97            et al., 2024). This report proposes an arrayed constellation of spacecraft spanning both  
 98            multiple latitudes *and* longitudes, i.e. a “CubeSwarm”. The reconstruction method pri-  
 99            oritizes accurate flow representation interior to the constellation array and builds the  
 100            flow map using a set of electric potential ridges, ensuring electrostatic flow. These ridges  
 101            follow some definition of a single auroral arc boundary determined using morphological

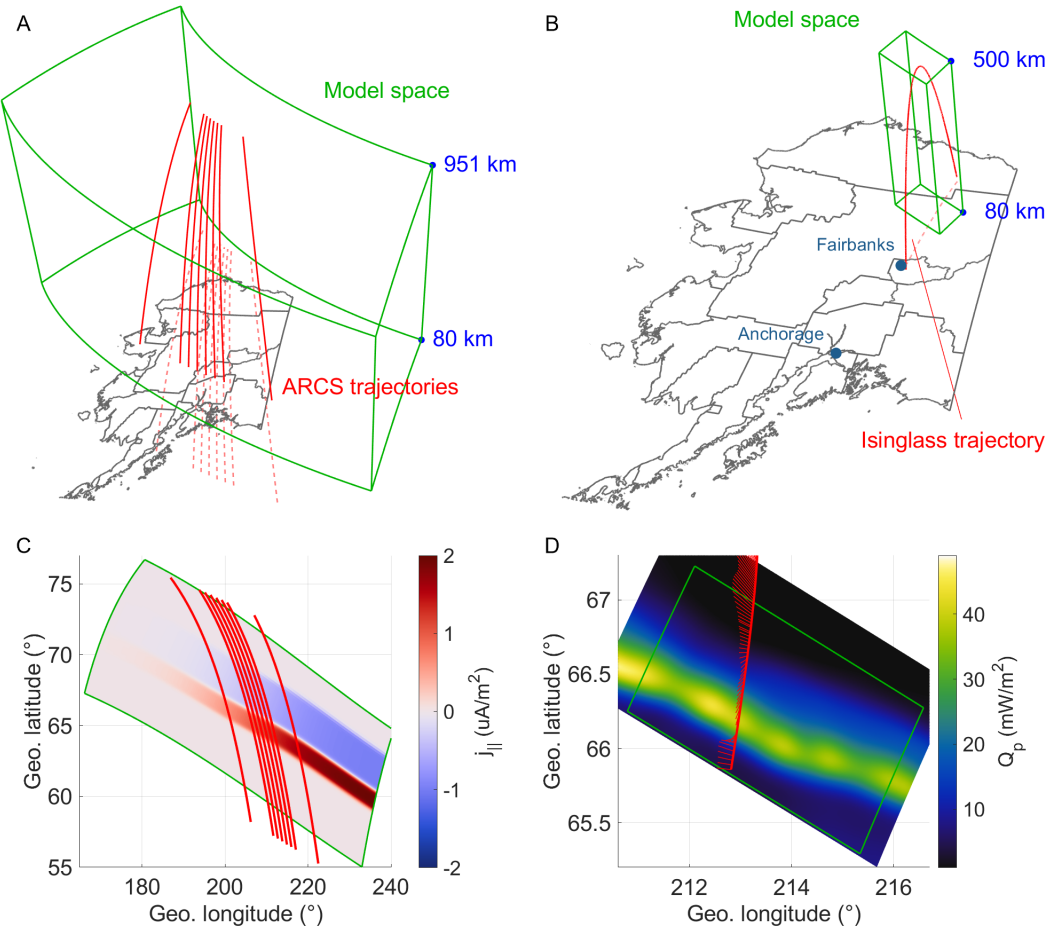


**Figure 1.** Context relating to the simulations used in demonstrating the reconstruction and replication methods. **A:** The simulation model space (green) and the ARCS trajectories (red) in reference to Alaska. **B:** Same as panel A but with the Isinglass trajectory. **C:** 2D FAC input map in reference to the model space (green). **D:** Total precipitating energy flux and plasma flow data in reference to the model space (green).

102 features of all-sky, multi-spectral imagery. The left column of Figure 1 outlines the con-  
 103 text of the Observing System Simulation Experiment (OSSE) used to demonstrate the  
 104 reconstruction technique. This OSSE is interpolated with virtual spacecraft to provide  
 105 fictitious plasma flow data.

106 The second method, “replication”, outlined in Section 2.2, stems from similar method-  
 107 ology outlined by Clayton et al. (2019, 2021) who use data from the Isinglass sounding  
 108 rocket campaign P.I. K. A. Lynch in conjunction with imagery from the UAF Geophys-  
 109 ical Institute’s Poker Flat Digital All-Sky Camera (DASC) dasc data ref . This method  
 110 makes use of plasma flow data from a single crossing, whether from a sounding rocket  
 111 (Clayton et al., 2019, 2021), spacecraft swarm data ref tii aurora archer maybe , or mesoscale  
 112 radar pfisr ref recent aurora . Here, the data are replicated, scaled, and rotated in ac-  
 113 cordance with *two* auroral arc boundaries, again, determined through all-sky imagery  
 114 features. The right column of Figure 1 shows the context of the simulation used to demon-  
 115 strate the replication technique.

The third method, a permutation of the second named “weighted replication”, is outlined in Section 2.3 and uses two (or more) tracks in conjunction with the all-sky imagery. This method repeats part of the replication methodology for each track and performs a weighted averaging on the interpolated flow maps (prior to enforcing electrostatics) with the weighting being based on the geometric distances to either track.

In all three methods, one of the main difficulties in creating a continuous plasma flow map lies in the constraint that it is divergence-less, i.e. electrostatic (Ruohoniemi et al., 1989; Nicolls et al., 2014). Vector fitting algorithms exist which handle this constraint, but will often provide large vortices to act as sources/sinks, replacing points of divergence/convergence refs .

## 2.1 Reconstruction

This section provides a proof-of-concept reconstruction using an OSSE used by Lynch et al. (2024) in where a localized “CubeSwarm” of virtual spacecraft scrape data from a 3D auroral arc simulation as they orbit through (see Figure 1A). The simulation used in this section is data inspired, but idealized; it is driven with a single pair of FAC sheets that have a slight bend in their profile and fade westward from  $\pm 1$  to  $0 \mu\text{A}/\text{m}^2$  over the span of the model space (see Figure 1C). The precipitation input maps are of a similarly shaped arc embedded within the poleward FAC sheet peaking at an energy flux of  $3 \text{ mW}/\text{m}^2$  and characteristic energy of 3 keV with gradient scale lengths of 40 km.

### 2.1.1 Reconstruction algorithm

With hindsight into what the form of the electric potential map is, and to avoid large plasma flow vortices, we construct the potential map out of a sum a user-defined number,  $N_k$ , of pseudo-basis functions each governed by a set of parameters. The functional form of each of them is an inclined Gaussian ridge, i.e. a Gaussian profile northward that extrudes east- and westward with a constant sloped amplitude, while following the boundary of the arc. This is done to find potential solutions that priorities across-arc gradients while remaining relatively unstructured along the arc. The  $\mathbf{E} \times \mathbf{B}$  plasma flow derived from this potential field is then compared against the virtual plasma flow data and their mean square differences are then minimized over the parameter space.

The arc boundary is determined using standard Sobel edge detection (Sobel, 2014). Given the idealistic nature of the OSSE used in demonstrating this method, this suffices, but we want to caution the reader regarding the complexities of determining less ideal arc boundaries. In any case, after determining an appropriate set of boundary points, they are least-squares fit against the following functional form:

$$b(x; \bar{A}) = \sum_{j=1}^{N_j} \left[ A_{j1} + A_{j2} \tanh\left(\frac{x - A_{j3}}{A_{j4}}\right) \right], \quad (2)$$

with  $\bar{A}^0$  being the  $N_j \times 4$  best fitting boundary parameter matrix,  $N_j$  the user-defined number of summation terms, and  $x$  the linear magnetic east coordinate. The choice of summing hyperbolic tangents lies in the tendency of auroral arcs to be aligned magnetic east-west and relatively unstructured in this direction.

With this, we define our pseudo-basis potential ridge as

$$\phi_k(\mathbf{r}; \bar{P}, \bar{A}) = (P_{k1}x + P_{k2}) \exp\left[-\frac{(y - P_{k3} - b(x; \bar{A}))^2}{P_{k4}^2}\right], \quad (3)$$

155 where  $\bar{P}$  is the  $N_k \times 4$  potential parameter matrix and  $y$  being the linear magnetic north  
156 coordinate, giving a total potential field of

$$\phi(\mathbf{r}; \bar{P}, \bar{A}) = \sum_{k=1}^{N_k} \phi_k(\mathbf{r}; \bar{P}, \bar{A}). \quad (4)$$

157 Prior work by [ref tucker](#) aimed to instead warp the flow field via a coordinate transfor-  
158 mation to along/across-arc coordinates, similar to those used by Marghitu (2012), but  
159 we have found the solution used here to be both simpler to implement and faster.

160 The plasma flow data from the virtual spacecraft provide the vectors  $\mathbf{v}_i = (v_{xi}, v_{yi})$   
161 at positions  $\mathbf{r}_i = (x_i, y_i)$  with  $i$  being the sample number. Generally, this flow data would  
162 require some mindful Gaussian smoothing, but more on this in Section [s:caution](#). With  
163 this, the electric field components to be compared against the plasma flow data are

$$\begin{aligned} E'_x(\mathbf{r}_i; \bar{P}, \bar{A}) &= -\frac{\partial}{\partial x} \phi(\mathbf{r}; \bar{P}, \bar{A}) \Big|_{\mathbf{r}_i} \\ &= -\sum_{k=1}^{N_k} \left[ P_{k1} + \frac{2\gamma(\mathbf{r}_i; \bar{P}, \bar{A})}{P_{k4}^2} (P_{k1}x_i + P_{k2}) \frac{\partial b}{\partial x} \Big|_{x_i} \right] \exp \left[ -\frac{\gamma(\mathbf{r}_i; \bar{P}, \bar{A})^2}{P_{k4}^2} \right] \end{aligned} \quad (5)$$

$$\begin{aligned} E'_y(\mathbf{r}_i; \bar{P}, \bar{A}) &= -\frac{\partial}{\partial y} \phi(\mathbf{r}; \bar{P}, \bar{A}) \Big|_{\mathbf{r}_i} \\ &= \sum_{k=1}^{N_k} \frac{2\gamma(\mathbf{r}_i; \bar{P}, \bar{A})}{P_{k4}^2} (P_{k1}x_i + P_{k2}) \exp \left[ -\frac{\gamma(\mathbf{r}_i; \bar{P}, \bar{A})^2}{P_{k4}^2} \right], \end{aligned} \quad (6)$$

164 with  $\gamma(\mathbf{r}; \bar{P}, \bar{A}) = y - P_{k3} - b(x; \bar{A})$  and

$$\frac{\partial b}{\partial x} = \sum_{j=1}^{N_j} \frac{A_{j2}}{A_{j4}} \operatorname{sech}^2 \left( \frac{x - A_{j3}}{A_{j4}} \right). \quad (7)$$

165 From here, with  $\mathbf{B} = -B\hat{z}$  and  $z$  the linear magnetic up coordinate, we rotate the elec-  
166 tric field providing plasma flow:

$$\mathbf{v}'(\mathbf{r}; \bar{P}, \bar{A}) = (v'_x, v'_y, 0) = \frac{\mathbf{E}' \times \mathbf{B}}{B^2} = \frac{1}{B} (-E'_y, E'_x, 0). \quad (8)$$

167 This reduces the problem to finding the parameter matrix,  $\bar{P}^0$ , which solves

$$\min_{\bar{P}} \sum_i [(v'_x(\mathbf{r}_i; \bar{P}, \bar{A}^0), v'_y(\mathbf{r}_i; \bar{P}, \bar{A}^0)) - (v_{xi}, v_{yi})]^2, \quad (9)$$

168 such that, with the optimized parameter matrix, the continuous plasma flow map is given  
169 by

$$\mathbf{v}_c(\mathbf{r}) = \mathbf{v}'(\mathbf{r}; \bar{P}^0, \bar{A}^0) \quad (10)$$

170 and subsequently the continuous potential map used to drive ionospheric models is

$$\phi_c(\mathbf{r}) = \phi(\mathbf{r}; \bar{P}^0, \bar{A}^0). \quad (11)$$

171 By using the potential ridges, we prioritize solutions for  $\phi_c$  that have sheet-like morphol-  
172 ogy in contrast to what has been done before (Kamide et al., 1981; Amm, 1997; Nicolls  
173 et al., 2014; Bristow et al., 2016; Laundal et al., 2022).

### 174 2.1.2 Reconstruction example

175 Figure 2 shows an example usage of the reconstruction algorithm. This example  
176 was developed for ARCS (Lynch et al., 2024) to verify the ability of plasma flow recon-  
177 struction given a local grouping of spacecraft. The virtual orbits are arranged densely  
178 to be able to provide map of along- and across-arc gradients.

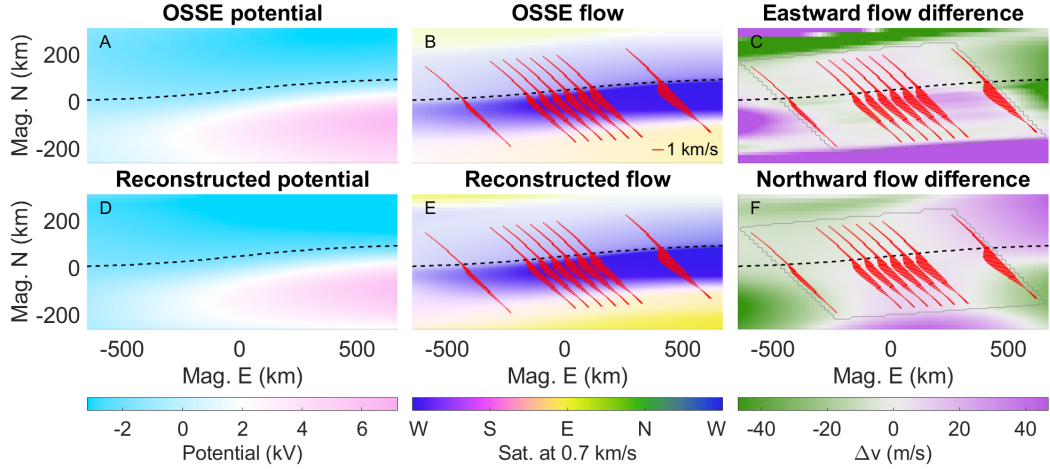


**Figure 2.** Example of a plasma flow field reconstruction. **A:** The electric potential map used to drive the OSSE with the boundary,  $b$ , overlaid. **B:** The resulting flow field with the virtual flow data points (red),  $\mathbf{v}_i$ , interpolated from it. The color representation of flow has the direction depicted by hue and the intensity by the color saturation. **D, E:** The reconstructed electric potential and flow. **C, F:** The difference between the reconstructed and OSSE east- and northward flow.

The black dashed lines are the imagery derived boundary,  $b$ , and the bag of plasma flow vectors,  $\mathbf{v}_i$ , is overlaid in red. The reconstructed electric potential,  $\phi_c$ , and reconstructed flow,  $\mathbf{v}_c$ , match well within the spacecraft region (gray outline in Fig. 2C, F) as per design. The maximum absolute flow difference in this region is 47 m/s eastward and 28 m/s northward with averages of 5(12) and 5(8) m/s. Outside the region, however, the error quickly ramps up due to the under-regulated potential ridge parameters,  $\bar{P}$ .

### 2.1.3 Possible improvements

Note about how we're moving on from this, but here are possible improvements one could do. Proper regularization on the potential ridges,  $\phi_k$ , can be used to stretch the region of good fit as presently the goodness-of-fit rapidly decreases when moving out of the spacecraft region. Furthermore, the electric field resulting from a single ridge i.e. Eqs. (5-6), far from the fitting region is

$$\lim_{\mathbf{r} \rightarrow \infty} E_{xk}(\mathbf{r}; \bar{P}, \bar{A}) = -P_{k1} \exp \left[ -\frac{(y - P_{k3} - b_{\pm\infty})^2}{P_{k4}^2} \right] \quad (12)$$

$$\lim_{\mathbf{r} \rightarrow \infty} E_{yk}(\mathbf{r}; \bar{P}, \bar{A}) = \frac{2}{P_{k4}^2} (P_{k1}x + P_{k2})(y - P_{k3} - b_{\pm\infty}) \exp \left[ -\frac{(y - P_{k3} - b_{\pm\infty})^2}{P_{k4}^2} \right], \quad (13)$$

where  $b_{\pm\infty} = \sum_j (A_{j1} \pm A_{j2})$  and  $\partial b / \partial x (x \rightarrow \pm\infty) \rightarrow 0$ . Clearly,  $E_{xk}$  remains finite, but  $E_{yk}$  diverges as  $|y| < \infty \wedge x \rightarrow \infty$ . Granted we work within the bounds of the model space, but slowing down this divergence would aid in regularization and smoother solutions. In actuality, models often require a good amount of buffer surrounding the region of interest into which the flow map needs to extrapolate. Lastly, incorporating weighted fitting would provide error estimates for reconstructions from real data as opposed to an OSSE, e.g. weights of  $w_i = 1/\sigma_i^2$  with  $\sigma_i$  being instrument error assuming a diagonal measurement covariance matrix.

201            **2.2 Replication**

202         The second method of developing continuous plasma flow maps uses plasma flow  
 203         data with approximately across-arc tracks in conjunction with all-sky, multi-spectral im-  
 204         agery. In this method, data is replicated along-arc using direct and indirect information  
 205         from the imagery. Primary *and* secondary boundaries are determined along which the  
 206         track data is translated, scaled, and the flow data is rotated to be tangent with the pri-  
 207         mary boundary. The example used here uses data set “c5” from Clayton et al. (2021).

208            **2.2.1 Arc boundary definitions**

209         Determining the arc boundaries from multi-spectral imagery data firstly requires  
 210         an inversion (ref) to a map of total energy flux,  $Q_p$ , and characteristic energy,  $E_p$ , of the  
 211         precipitating electrons. From these a proxy for the Pedersen conductance is made which,  
 212         at the time of writing, is done using Eq. (3) by Robinson et al. (1987):

$$\Sigma_P(x, y) = \frac{40(E_p(x, y)/\text{keV})}{16 + (E_p(x, y)/\text{keV})^2} \left( Q_p(x, y)/\text{mW/m}^2 \right)^{1/2}. \quad (14)$$

213         The reader is cautioned, however, to use multi- and/or two-stream transport mod-  
 214         els, such as the GLobal airglOW (GLOW) model (Solomon, 2017), or look-up tables gen-  
 215         erated by such models, to determine a more accurate Pedersen conductance.

216         With this, the primary and secondary arc boundaries are established in one of two  
 217         ways on *either* the total energy flux *or* Pedersen conductance: 1) finding the magnetic  
 218         latitude of the first two most prominent edges at each magnetic longitude using Sobel  
 219         edge detection (Sobel, 2014) in the magnetic northward direction, or 2) following a con-  
 220         tour line at two isovalues which can be chosen directly, or determined at the locations  
 221         of the central two most prominent edges along the track. *In either case, the boundary*  
 222         *is Gaussian smoothed. should we do this? Is it harder to find a laminar flow solution with*  
 223         *less smoothing? Is there an anti-correlation to curliness and boundary smoothing? Do*  
 224         *more wiggly arcs have more hall closure, or is the penalty more curl of A?* Figure 3 shows  
 225         the Pedersen conductance and its magnetic northward Sobel convolution along with the  
 226         primary and secondary boundaries determined using method 2 with Pedersen conduc-  
 227         tance and method 1 with total energy flux. In the remainder of this paper, we use bound-  
 228         aries determined using Pedersen conductance contour lines.

229            **2.2.2 Flow data replication**

230         Firstly, the plasma flow data track is Gaussian smoothed (more on this in Section  
 231         ref section ) and, prior to doing any replication, we split the flow field into two compo-  
 232         nents: 1) the background flow treated as a constant, large-scale, global disturbance, and  
 233         2) the small-scale disturbances imposed by the arc itself:

$$\mathbf{v}(\mathbf{r}) = \mathbf{v}_{\text{arc}}(\mathbf{r}) + \mathbf{v}_{\text{bg}}. \quad (15)$$

234         In absence of background flow, the most basic model of an auroral arc is composed  
 235         of only across-arc flow shear, i.e. electric field shocks (Marghitu, 2012). Thus, we define  
 236         the background flow such that, once removed, the flow at the intersection of the track  
 237         and the primary boundary is tangent to that boundary. Furthermore, this simplistic model  
 238         has the arc defined as a band of enhanced conductance in which we expect the electric  
 239         field to quench. Thus, it makes sense to replicate this data along the arc boundaries, while  
 240         remaining tangent to it, and scaling such that the shorted out electric fields remain in-  
 241         side the area of enhanced conductance. This leads to the following plasma flow data track  
 242         replication algorithm:

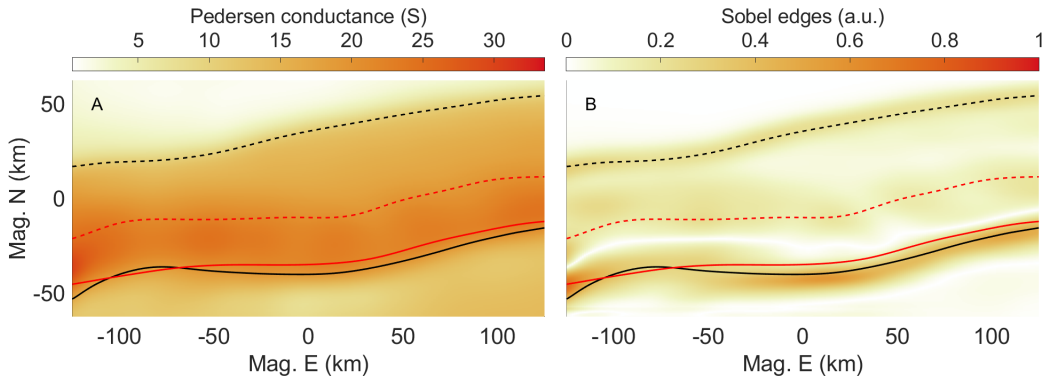


**Figure 3.** Primary (solid) and secondary (dashed) boundaries using Pedersen conductance and contour lines at 19.1 S and 10.5 S (black). In red are the boundaries determined using the energy flux (not shown) with the steepest gradient method. **A:** Pedersen conductance determined via Eq. (14). **B:** Magnetic northward Sobel convolution of the Pedersen conductance. Both sets of boundaries have an approximate smoothing window of 15 km.

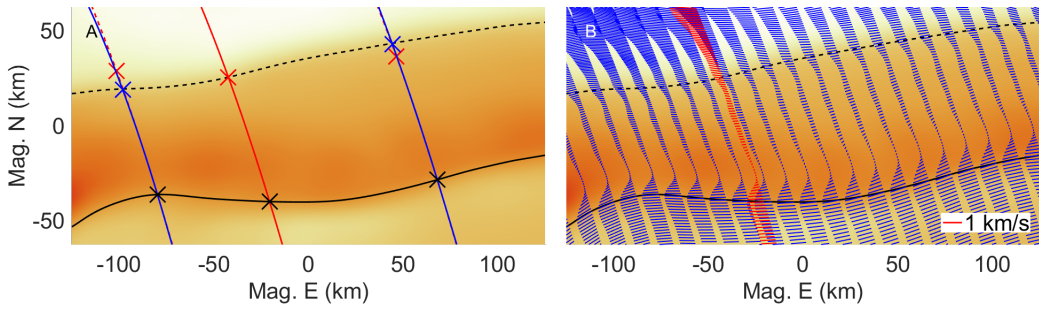


**Figure 4.** In situ trajectory flow data replication overlaid on the same conductance map from Figure 3A. **A:** Two example replications (blue) of the original trajectory (red) along the primary arc boundary (solid black). The black crosses have the same flow data. The red/blue crosses indicate flow data before/after scaling to meet up with the secondary arc boundary (dashed black). **B:** A low density replication (blue) along with the original, smoothed flow data (red).

- 243 1. The original track is translated by some amount following the primary arc bound-  
244 ary such that the original and replicated flow data are equal at the primary boundary-  
245 track intersections.  
246 2. The replicated track is scaled in the along-track direction such that the original  
247 and replicated flow data are equal at the secondary boundary-track intersections.  
248 3. The flow data of the replicated track is rotated by a constant angle per track such  
249 that it remains to be tangent to the primary arc boundary.  
250 4. Repeat this replication for multiple translations along the arc until the 2D model  
251 space is filled with a replication rate higher than the eastward Nyquist spacing.

252 Figure 4 illustrates these steps given the boundaries of Figure 3. The left panel shows  
253 two examples of how replications of the original trajectory are translated and scaled. The  
254 western replication example is scaled down to have the data at the red cross meet the  
255 secondary boundary, while the eastern replication is scaled up to do the same. The right  
256 panel shows the replication, but done only for a few instances for illustration purposes.  
257 This also shows the rotated flow vectors keeping tangent with the primary boundary.

258      **2.2.3 Enforcing electrostatic flow**

259      Next, the replicated flow data is interpolated onto the model grid. This section out-  
 260      lines three choices of fitting an electric potential map to this interpolated flow field,  $\mathbf{v}_{\text{arc}} =$   
 261       $\mathbf{E}_{\text{arc}} \times \mathbf{B} / B^2$ , where  $\mathbf{B}$  is the magnetic field from Eq. (8) and  $\mathbf{E}_{\text{arc}}$  is the arc disturbed  
 262      ionospheric electric field perpendicular to  $\mathbf{B}$ . The interpolated flow fields' associated elec-  
 263      tric field reads as follows:

$$\mathbf{E}_{\text{arc}}(\mathbf{r}) = -\mathbf{v}_{\text{arc}}(\mathbf{r}) \times \mathbf{B} = \mathbf{E}_I(\mathbf{r}) + \mathbf{E}_S(\mathbf{r}) = -\nabla\phi_c(\mathbf{r}) + \nabla \times \mathbf{A}(\mathbf{r}), \quad (16)$$

264      where  $\phi_c$  is the electric potential map we're looking for and  $\mathbf{A}$  is the magnetic vector po-  
 265      tential. We want to remove the non-electrostatic part, i.e. find the irrotational electric  
 266      field,  $\mathbf{E}_I$ , and remove the solenoidal field,  $\mathbf{E}_S$ , in a way that best agrees with the inter-  
 267      polated flow field. Three choices of doing so are as follows:

- 268      1. **Brute force:** Perform a least-squares fitting algorithm (Levenberg–Marquardt  
 269      in our case) that directly fits a potential map,  $\phi$ , i.e.

$$\min_{\phi} \|\nabla \times \mathbf{A}(\mathbf{r})\|_2^2 = \min_{\phi} \|\nabla\phi(\mathbf{r}) + \mathbf{E}_{\text{arc}}(\mathbf{r})\|_2^2 = \min_{\phi} \sum_{i,j} \left( (\nabla\phi)_{ij} + \mathbf{E}_{\text{arc},ij} \right)^2, \quad (17)$$

270      the solution of which,  $\phi_c$ , is the continuous potential map.

- 271      2. **Averaged path-integrated:** Average several path-integrated potential maps in  
 272      an attempt to drown out the non-conservative part of the interpolated field, i.e.

$$\phi_l(\mathbf{r}) = \int_{x_l}^x dx' \mathbf{E}_{\text{arc}}(x', y_l) \cdot \hat{x} + \int_{y_l}^y dy' \mathbf{E}_{\text{arc}}(x, y') \cdot \hat{y}, \quad (18)$$

273      where we take  $\phi_c = \langle \phi_l \rangle$ .

- 274      3. **Helmholtz decomposition:** Use the Fourier transform method for Helmholtz  
 275      decomposition (Mule, 2023, Pers. comm.). Taking the 2D Fourier transform of Eq. (16)  
 276      gives us

$$\mathbf{G}(\mathbf{k}) = -i\mathbf{k}G_{\phi}(\mathbf{k}) + i\mathbf{k} \times \mathbf{G}_{\mathbf{A}}(\mathbf{k}), \quad (19)$$

277      where  $\mathbf{k} = (k_x, k_y)$  is the wave vector and  $\mathbf{G}$ ,  $G_{\phi}$ , and  $\mathbf{G}_{\mathbf{A}}$  are the Fourier trans-  
 278      forms of  $\mathbf{E}_{\text{arc}}$ ,  $\phi_c$ , and  $\mathbf{A}$  respectively. Taking the dot product of Eq. (19) with  $\mathbf{k}$   
 279      gives us an expression for the Fourier transform of the potential:

$$G_{\phi}(\mathbf{k}) = i \frac{\mathbf{k} \cdot \mathbf{G}(\mathbf{k})}{\|\mathbf{k}\|^2}, \quad (20)$$

280      such that

$$\phi_0(\mathbf{r}) = \mathcal{F}^{-1}\{G_{\phi}(\mathbf{k})\} = \int_{-\infty}^{+\infty} dk_x \int_{-\infty}^{+\infty} dk_y G_{\phi}(\mathbf{k}) e^{i(xk_x + yk_y)}. \quad (21)$$

281      Here we've found the electric potential up to a harmonic function (i.e. gauge in-  
 282      variance). The potential map we want is  $\phi_c = \phi_0 + f$  where  $\nabla^2 f = 0$ . One choice  
 283      of  $f$  has the average electric field remain the same such that

$$f_a(\mathbf{r}) = \langle -\nabla\phi_0(\mathbf{r}) - \mathbf{E}_{\text{arc}}(\mathbf{r}) \rangle \cdot \mathbf{r}. \quad (22)$$

284      A second option for  $f$  solves the optimization problem

$$\min_{\bar{F}} \left\| -\nabla(\phi_0(\mathbf{r}) + f_b^m(\mathbf{r}; \bar{F})) - \mathbf{E}_{\text{arc}}(\mathbf{r}) \right\|_2^2 \quad \text{with } \mathbf{r} \in \mathcal{M}, \quad (23)$$

285      where  $\bar{F}$  is an  $m \times 2$  parameter matrix,  $\mathcal{M}$  is a user defined masking domain sur-  
 286      rounding the primary and/or secondary boundary, and original track, and  $f_b^m$  is

the most general  $m$  order polynomial in  $x$  and  $y$  that satisfies Laplace's equation:

$$f_b^m(\mathbf{r}; \bar{F}) = \sum_{n=1}^m \sum_{q=0}^{\lfloor n/2 \rfloor} (-1)^q \left[ \frac{F_{n1}}{\rho^{n-1}} \binom{n}{2q+1} x^{2q+1} y^{n-2q-1} + \frac{F_{n2}}{\rho^{n-1}} \binom{n}{2q} x^{2q} y^{n-2q} \right], \quad (24)$$

where  $\rho$  is a regularization parameter balancing higher order terms. To show this is the most general case, take the complex polynomial of degree  $m$

$$p(z) = \sum_{n=0}^m F_n^* z^n, \text{ where } z^n = (x + iy)^n = \sum_{q'=0}^n \binom{n}{q'} x^{q'} (iy)^{n-q'}, \quad (25)$$

and recognize that the homogeneous polynomial  $z^n$  is analytic which therefore has harmonic real and imaginary parts (Ahlfors, 1953). This gives two parameters, the real and imaginary parts of  $F_n^*$ , for each value of  $n$ . To show uniqueness, we recognize that the Laplacian maps homogeneous polynomials of degree  $n$  to those of degree  $n-2$ , the domain and image of which have dimensions  $n$  and  $n-2$  respectively. By the rank nullity theorem (Mule, 2024, Pers. comm.), this means the dimension of the kernel of the Laplacian is  $n - (n-2) = 2$ , so we've found all solutions. An example for  $m = 2$  and  $\rho = 10$  m gives

$$f_b^3(x, y, \bar{F}) = F_{11}x + F_{12}y + \frac{F_{21}}{10}(x^2 - y^2) + \frac{F_{22}}{10}xy. \quad (26)$$

Note that with  $q$  in meters and  $\bar{F}$  in V/m has  $f_b$  in volts. When solving for this optimization the initial guess is taken to be  $(f_2^m)_0 = f_a$ .

Along with the interpolated flow field (column 1), examples of the the brute force and Helmholtz decomposition methods are shown in Figure 5 (columns 2-3). The averaged path-integrated method is not shown as it does not perform as well, perhaps due to the accumulation of systematic error. The divergence panel shows that of the interpolated flow field and indicates the location of rotational signatures which are interpretable as Alfvénic. Although the brute force method is easiest to justify being the “best” fit, it is also by far the slowest, taking at least several hours on a clustered machine. The Helmholtz decomposition method, on the other hand, has the advantage of using the fast Fourier transform method and it compares reasonably well, even when using the direct harmonic solution,  $f_a$ . This is illustrated in Figure 6 which shows the residual between the brute force solution and the potential from Eq. (21) compared against a masked and unmasked harmonic fit. Clearly, a constant background electric field match, i.e. a harmonic function that is constant sloped plane,  $f_a$ , is a first order solution in this particular case but this requires further confirmation for other cases. The masking acts as a binary **placeholder** for a continuous instrument error based weighting map. Such an improved map will aid in constraining the potential in the corners of the model space (see Figure 6C).

**reviewer Q: if brute force so slow why not use reconstructor from previous section?**  
Even a 4x512 parameter matrix will be much faster than 128x256 cells. reconstructor is an early version of replicator, this can (and perhaps should) be used in place of the pseudo basis technique.

### 2.2.4 Replication example

Figure 7 shows the replication methodology applied to the “c5” example by Clayton et al. (2021) (see their Table 1). The top row has the scaling and rotating applied, whereas the bottom row is done with neither. Firstly, the applied scaling to the replication results in a co-location of the shorted out electric field and the auroral precipitation as seen by the  $\Sigma_P$  contour lines in panel A, in comparison to panel D. Secondly, the applied rotation provides more streamlined plasma flow, in the literal sense, as seen by the change from southwest to west to southwest flow in panel A. In contrast, without rotation the

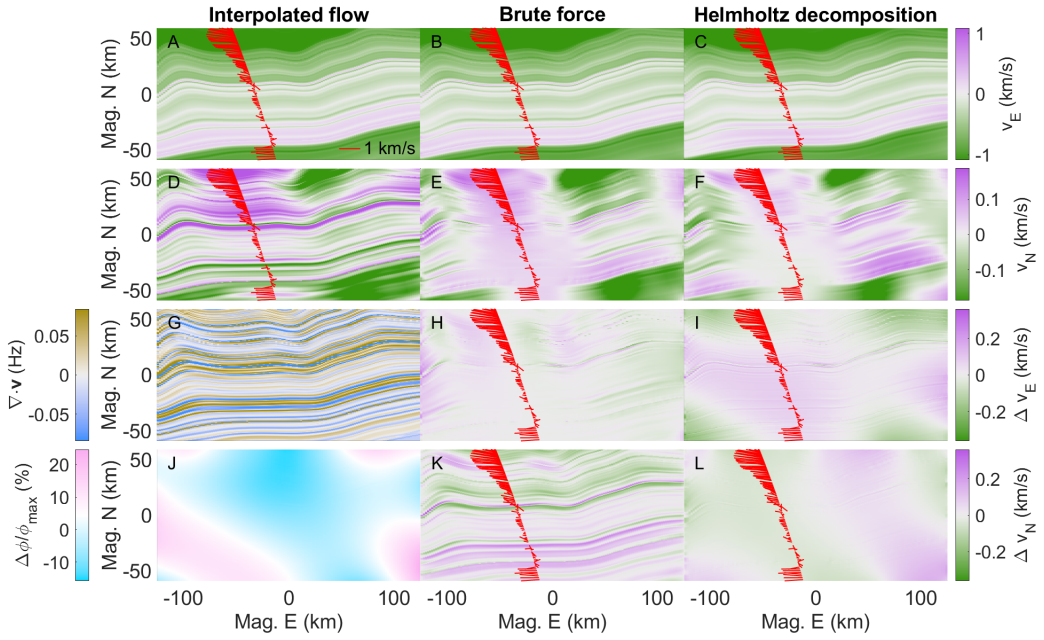


**Figure 5.** Comparison of fitting a potential map to an interpolated flow map,  $v_{\text{arc}}$ . **A-C:** Eastward interpolated, brute force fitted, and Helmholtz decomposed flow. **D-F:** Same but northward. **G:** Divergence of the interpolated flow. **H, K:** Difference in east and northward flow between brute force and interpolated. **I, L:** Difference in east and northward flow between Helmholtz decomposed and brute force. **J:** Relative difference in potential between brute force and Helmholtz decomposed. Needed?

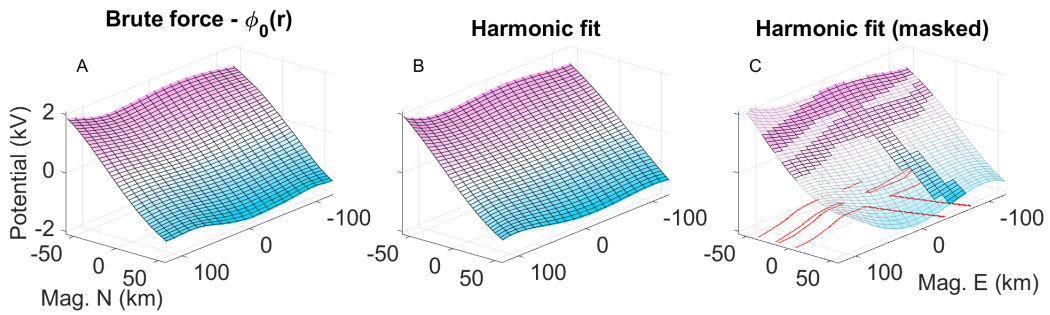


**Figure 6.** Validity of a harmonic function fit. **A:** Residual potential between brute force fitting and Eq. (21). **B:** Unmasked harmonic function fit from Eq. (24) with  $m = 5$  and  $q = 10$  m. **C:** Same as panel B but masked with the mask,  $\mathcal{M}$ , in red.

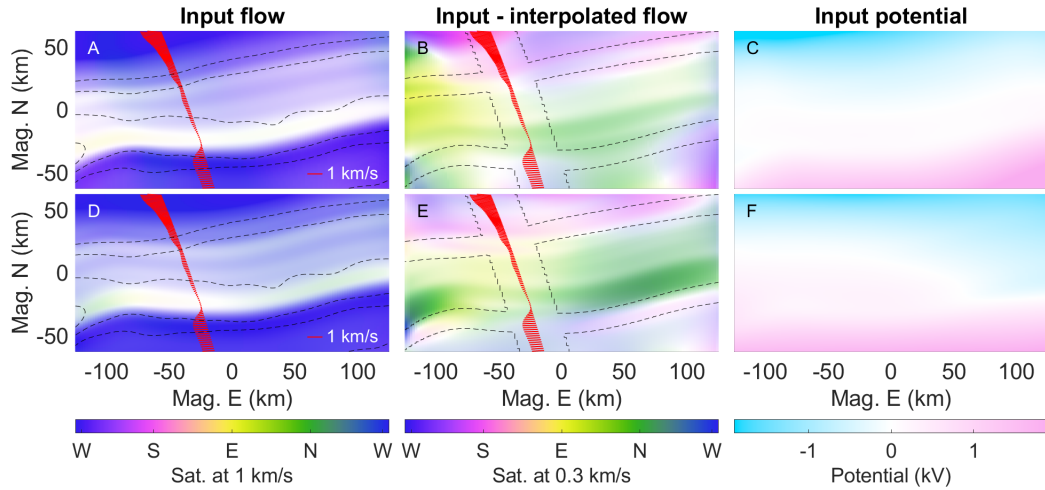


**Figure 7.** Input flow and potential maps used to drive simulations with (top row) and without (bottom row) replication scaling/rotating. **A, D:** Hue-saturation plots of  $-\nabla\phi_c$  with contour lines of  $\Sigma_P$ . **B, E:** Flow error, i.e.  $-\nabla\phi_c - \mathbf{v}_{\text{arc}}$ , with masking contours where the harmonic function is fit. **C, F:** Input potential maps,  $\phi_c$ .

flow remains westward resulting in a changing angle between the electric field and the conductance gradients. This has physical effects on auroral current closure (see Eq. (1)).

**Comment on qualitative performance.**

### 2.3 Weighted replications

In the event of a conjunction between auroral imagery and two flow data tracks, the replication method can simply be repeated up to the interpolation step. Both replications use the same primary and secondary boundaries as well as the same background flow,  $\mathbf{v}_{\text{bg}}$ . This background flow is determined by whichever replication is done first. The flow data smoothing is also performed with approximately equal Gaussian filter physical window widths.

Once both tracks have their replication and subsequent interpolated flow fields, they are weighted average with the weighting functions

$$w_A(\mathbf{r}) = \frac{1}{2} \left[ 1 + \tanh \left( \frac{d_{\min,B}(\mathbf{r}) - d_{\min,A}(\mathbf{r})}{s_w} \right) \right], \text{ and } w_B(\mathbf{r}) = 1 - w_A(\mathbf{r}). \quad (27)$$

Here,  $d_{\min,A}$  is a map of the shortest straight-line distances from points  $\mathbf{r}$  to track  $A$  and similarly for track  $B$ . This configuration of weighting allows for two intersecting tracks. The scale length,  $s_w$ , will introduce flow gradients and has to be chosen with care. From here we have a new interpolated arc-disturbed plasma flow,

$$\mathbf{v}_{\text{arc}}(\mathbf{r}) = w_A(\mathbf{r})\mathbf{v}_{\text{arc},A}(\mathbf{r}) + w_B(\mathbf{r})\mathbf{v}_{\text{arc},B}(\mathbf{r}), \quad (28)$$

from which the methodology from Section 2.2.3 takes over. This ensures electrostatics, but it should be mentioned that, on top of the divergences still remaining in either track's interpolated field, this weighting function introduces additional divergence of the form

$$(\nabla \cdot \mathbf{v}_{\text{arc}})_w = \nabla w_A(\mathbf{r}) \cdot (\mathbf{v}_{\text{arc},A} - \mathbf{v}_{\text{arc},B}). \quad (29)$$

This weighting function, however, has small northward gradients and the interpolated flows are expected to not vary much eastward, i.e.  $\nabla w_A$  is approximately orthogonal to

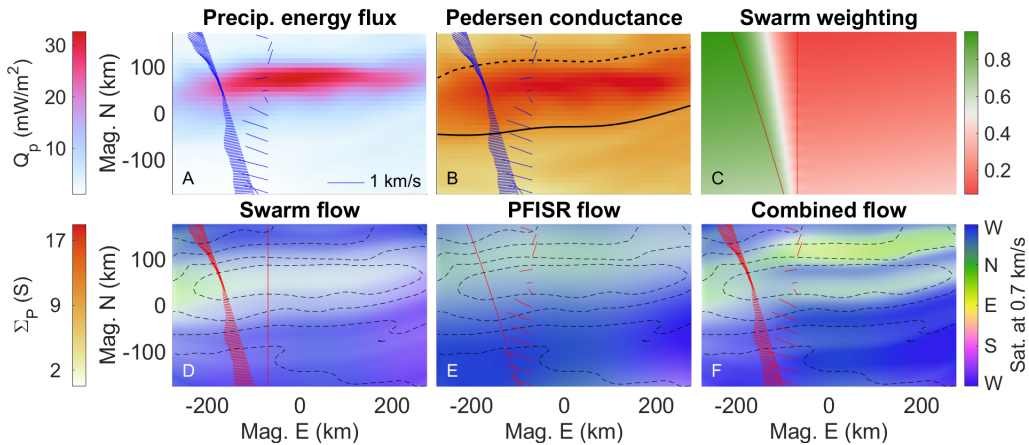


**Figure 8.** Weighted replication example. **A:** Precipitating total electron energy flux with plasma flow data from Swarm (left trajectory) and PFISR (right track) in blue. **B:** The GLOW derived Pedersen conductance with the primary (solid) and secondary (dashed) boundaries overlaid. **C:** The weighting map,  $w_A$ , used for the Swarm data with a scale length of  $s_w = 200$  km. **D-F:** Resulting flow maps from using only Swarm data, only PFISR data, and from using both datasets, respectively.

$\mathbf{v}_{\text{arc},A} - \mathbf{v}_{\text{arc},B}$  resulting in minimal diverging flow. This ensures that the Helmholtz decomposition provides an electrostatic solution of the final flow map that doesn't stray far from the interpolated flow map.

For more than two replications the weighting function requires some adjustments, but this is also perfectly possible.

### 2.3.1 Weighted replication example

To illustrate the double replication methodology, a conjunction from the *Swarm-over-Poker-2023* campaign is used (Feb - March 2023, Poker Flat Research Range, AK). This campaign facilitated conjunctions of (among a variety of other data) ion flow data from the Thermal Ion Imagers (Knudsen et al., 2017) on ESA's Swarm mission, convection flow data from AMISR's Poker Flat Incoherent Scatter Radar (PFISR) (Kelly & Heinselman, 2009; Nicolls & Heinselman, 2007; Heinselman & Nicolls, 2008), and multispectral, all-sky imagery from the Poker Flat DASC [dasc data ref](#). This campaign has developed a growing collection of heterogeneous auroral observations for the winter months of 2023. Our example uses data from March 19 at 8:23:44 UT (20.5 MLT).

Figure 8A summarizes this event showing a  $Q_p \approx 30$  mW/m<sup>2</sup> (with  $E_p \approx 7$  keV, not shown) auroral arc with some along-arc structure. The left trajectory shows flow data from Swarm B and the right track shows that from PFISR. Panel B also shows the Pedersen conductance (this time derived using GLOW (Solomon, 2017)) which is used to determine the arc boundaries and panel C shows the weighting function used for the Swarm data. The bottom row gives the final continuous plasma flow maps when using only the Swarm data, or the PFISR data, or both. The individual reconstructions are dissimilar, but this is to be expected given the along-arc structure. Note about how swarm B data was constructed (ask Alex).

### 373 3 Driving GEMINI with the Replication Method

#### 374 3.1 The GEMINI model

375 To investigate the effects of continuous plasma flow maps in conjunction with au-  
 376 roral precipitation, we use state-of-the-art 3D ionospheric simulations provided by the  
 377 Geospace Environment Model of Ion-Neutral Interactions (GEMINI) (M. D. Zettergren  
 378 & Semeter, 2012; M. Zettergren & Snively, 2019). This is a multi-fluid (6 ions + elec-  
 379 trons), quasi-electrostatic model with its particle continuity consisting of chemical pro-  
 380 duction/loss and photo/impact ionization. Calculations of local densities, plasma flows,  
 381 and temperatures are treated self-consistently and the model includes thermal con-  
 382 duction heat flux, collisional heating, thermoelectric electron heat flux, and inelastic cool-  
 383 ing/heating from photoelectrons. This is supplemented with Maxwell's equations and,  
 384 at the time of writing, includes no displacement current or magnetic induction effects.  
 385 With this, the system is solved through enforcing divergence-less currents, curl-free elec-  
 386 tric fields, and invoking Ohm's law. Note: coming this fall: adaptive mesh refinement  
 387 and neutral coupling!

#### 388 3.2 Simulation examples

389 Figure 9 depicts GEMINI output data with Figure 7C as the flow driver and the  
 390 same precipitation data used by example “c5” from Clayton et al. (2021). The calculated  
 391 topside FAC slice is taken at an altitude of 200 km, but is translated down to 80 km for  
 392 visualization purposes. In order to visualize FAC closure, we opt for current flux tubes  
 393 which are made possible by the enforced condition of  $\nabla \cdot \mathbf{j} = 0$  and the use of stream-  
 394 lines sourced at closed elliptical curves (solid black curves). This enables an intuitive in-  
 395 terpretation of auroral current closure by showing where a patch of FAC joins back with  
 396 the magnetosphere or where a region of Hall current ends up. The dotted black and blue  
 397 curves show the projection of the terminating ends of the flux tubes onto the FAC map.  
 398 The green flux tube (28.4 kA) is a stereotypical example of FAC closure via the Peders-  
 399 sen layer, closing down between 118 - 154 km. The orange tube ( XX kA) runs under-  
 400 neath it and shows exchange between a region of Hall current and Pedersen current up  
 401 near the bottom of the Pedersen layer. This tube spans between 87 - 105 km in altitude  
 402 at its lowest point, and exits the equatorward wall between 101 - 138 km. The red flux  
 403 tube (23.9 kA) is, to some extent, a combination of these two, and has two exit regions.  
 404 When this tube has its sourced downward FAC run out of upward FAC to close through  
 405 in its paired sheet, it continues onto the next upward FAC sheet poleward of it where  
 406 the remaining XX kA is closed.

407 To show the effects of steps 2 and 3 of section 2.2.2, the output from Figure 9 is  
 408 also simulated with the same precipitation maps, but with the replication scaling and  
 409 rotating turned off (see Figure 7D-F). Figure 10 divides the topside FAC maps of both  
 410 simulations into the three terms from Eq. (1) in order to look at the effects of the plasma  
 411 flow shear and precipitation gradients separately. Figure 10D shows sensible results given  
 412 a single arc boundary, but panels E and F illustrate an amalgamation of two apparent  
 413 arc profiles at the poleward edge of the arc. The rotation between the arc disturbed elec-  
 414 tric field and the Pedersen and Hall conductance gradients causes the secondary bound-  
 415 ary to substantiate through, even though these replications are fully transparent to this  
 416 second boundary.

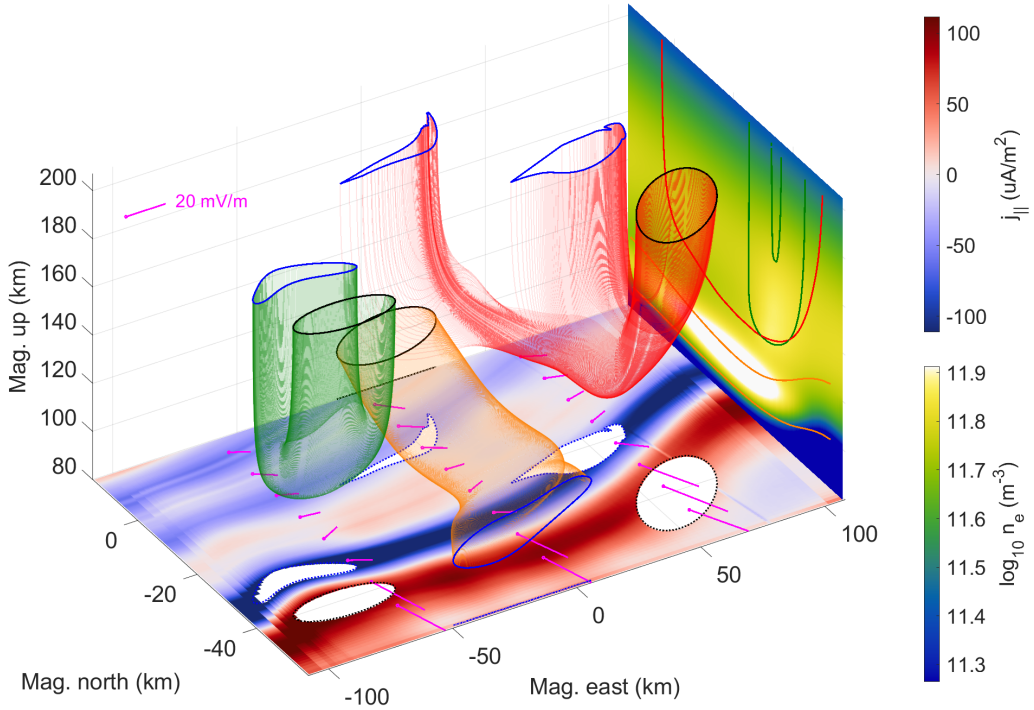


**Figure 9.** Plasma flow driven GEMINI output with input from the potential in Figure 7C. Current flux tubes are colored for distinction purposes and start/end at solid black/blue curves. The orange flux tube runs in reverse. **East side:** A north-up slice of electron density taken at 0 km east along with flux tube outline projections. **Bottom side:** An east-north slice of FAC (with parallel being down) taken at 200 km altitude along with flux tube start/end curve projections and electric field vectors (magenta). Note that these vectors include the background electric field.

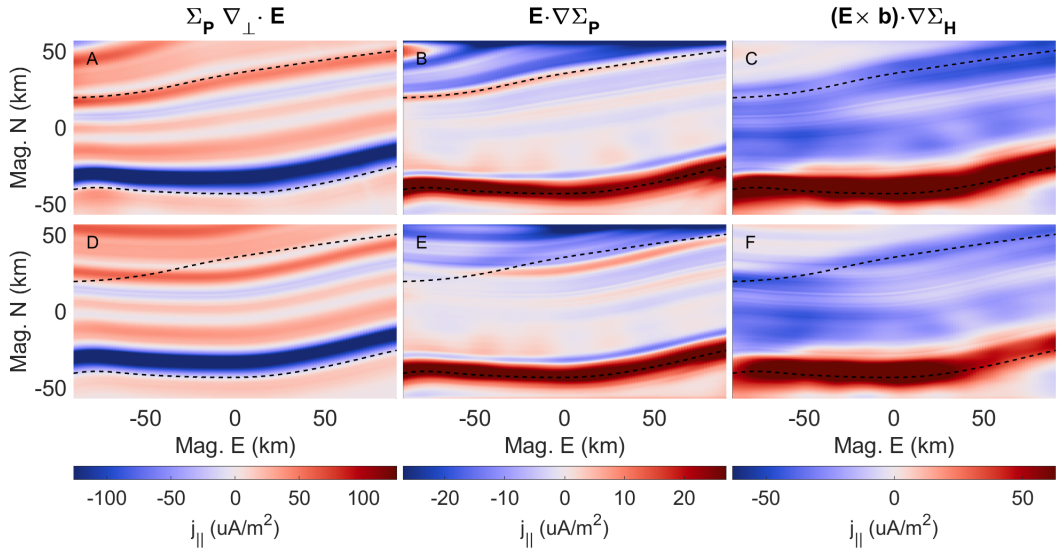


**Figure 10.** Calculated FAC components from Eq. (1). **A-C:** Terms 1 through 3 respectively split from the FAC map shown in Figure 9 along with arc boundaries (dashed). **D-E:** Same as the top row but with replication scaling and rotating turned off.

417 **4 Discussions**

418 **4.1 Improvements to auroral plasma flow mapping**

419 **Why do we need 3D simulations?** Figure 9 indicates that even for one of the most  
 420 basic examples of an auroral arc system, the morphology of current closure is 3D in nature.  
 421 The green flux tubes depicts a more instinctive auroral current closure type using  
 422 largely Pedersen currents to close (Mallinckrodt, 1985), however, the red flux tube illus-  
 423 trates a less common view of FAC current closure; not all current from one FAC sheet  
 424 has to close with its neighbouring sheet. This tube “digs” deeper into the Hall layer, sub-  
 425 sequentially rotating, in search of another closure path. Secondly, the orange flux tube is  
 426 mostly Hall current, but includes divergence, i.e. the last term in Eq. (1), being fed into  
 427 Pedersen currents as the tube climbs to reach higher conductivity (see the electron den-  
 428 sity panel). This Pedersen current can no longer be used to close FACs, which is how  
 429 diverging Hall currents can indirectly effect  $j_{\parallel}$ . Additionally, FAC closure is not restricted  
 430 to the Pedersen or Hall layers at around 90 - 130 km; depending on the perpendicular  
 431 distance from the FAC sheet inflection line, FACs can close as high as 144 km. This hap-  
 432 pens because, despite lower conductivity at high altitudes, the flux is conserved by in-  
 433 creasing the altitudinal range of the closure section of the tube.

434 All of this 3D structure is attributable to the interplay of the altitude dependent  
 435 Pedersen and Hall conductivities as a region of current attempts to find the path of least  
 436 resistance. To better understand quasistatic auroral arc scale science, and the non-passive  
 437 role the ionosphere plays in MI coupling, these 3D features require further studies, which  
 438 in turn requires 3D auroral simulations and, in turn, electrostatic, continuous, 2D, top-  
 439 side F-region boundary maps.

440 **How have we improved making 2D auroral arc drivers?** We have developed tech-  
 441 niques for creating such maps which focus on auroral physical and gradient scale lengths,  
 442 and discrete sheet-like morphologies. [sentence about reconstruction](#). The replication  
 443 methodology aims to use maximal information from the 2D precipitation maps to get  
 444 the most intuitive plasma flow map possible. To do so, and as improvements to work done  
 445 by (Clayton et al., 2019), we use:

- 446 1. imagery derived Pedersen conductance contour lines, in place of energy flux gra-  
 447 dents, as a more natural choice for copying electric field data
- 448 2. a secondary auroral arc boundary to which the plasma flow data is scaled in an  
 449 attempt to co-locate shorted-out electric fields with enhanced precipitation
- 450 3. plasma flow rotation to ensure the zeroth order electric field shock definition of  
 451 auroral arcs

452 Figure 7 and 10 demonstrate these improvements. These additional measures ensure that  
 453 the directions of the electric fields and the image related gradients are more intuitive,  
 454 and they are the next step towards studying auroral arcs that stray from their ideal, sheet-  
 455 like morphologies.

456 **4.2 Cautionary remarks**

457 The Gaussian smoothing of the plasma flow data (referred to in Section 2.2.2) should  
 458 not be arbitrary. Eq. (1) shows that the gradient in the track direction directly affects  
 459 the magnitude of the FAC provided by the first term. The resolution of the optical data  
 460 (often the limiting resolution [A. Mule is improving this](#)) should determine the scale length  
 461 of the Gaussian filtering of the plasma flow data in such a way that the Pedersen and  
 462 Hall conductance gradient terms match the diverging electric field term in Eq. (1). For  
 463 example, Figure 8 shows a precipitation and conductance map that are of similar gra-  
 464 dient scale lengths to that of the resulting plasma flow maps. As a validation check, the  
 465 area integral of the model calculated FAC map over the region of interest should approx-

466 imately vanish. In the case both Pedersen and Hall conductances are available, this check  
 467 can also performed prior to simulating.

468 As a second cautionary reminder, the replicated plasma flow interpolation (see Section  
 469 2.2.3) needs to be done using cubic or cubic spline methods to ensure a continuity  
 470 of  $C^1$  or higher. Using linear interpolation results in strong rippling of simulated FAC  
 471 due to discontinuous first derivatives of the electric field.

## 472 5 Conclusions and future work

473 Measurements of auroral arc systems can be sparse, heterogeneous, and largely dis-  
 474 tributed, while ionospheric models generally require continuous 2D input drivers. We  
 475 have circumvented this limitation by using extensive information from multi-spectral,  
 476 all-sky imagery. We have outlined three empirical methods for creating electrostatic, con-  
 477 tinuous, 2D, topside F-region convection boundary conditions that focus on typical sheet-  
 478 like discrete auroral arc structures. The main takeaways are as follows:

- 479 1. Even for the most basic auroral arc systems, a 2D description is insufficient and  
   hides the 3D nature of current closure.
- 480 2. When extrapolating F-region plasma flow data surrounding auroral arcs, it is im-  
   portant to scale the data in a way that co-locates the associated shorted out elec-  
   tric fields with the region of enhanced conductance.
- 481 3. Similarly, it is important to rotate the plasma flow data to avoid introducing un-  
   intuitive angles between the ionospheric electric field and the conductance gradi-  
   ents.

### 487 5.1 Future work

488 This work will be used to address the question of “what self-consistency constraints  
 489 exist in creating a geophysically coherent set of F-region, quasistatic auroral system drivers?”.  
 490 Finding a set of electrostatic auroral conductances, convection flow, and FAC maps that  
 491 are physical and self-consistent is fully determined by Eq. (1). Finding a set that appears  
 492 in nature, on Earth, and is likely requires more intuition and understanding of the in-  
 493 terplay between these three ingredients. The techniques outlined in this paper will be  
 494 used to develop a sub-catalog of data driven 3D simulations provided by events from the  
 495 *Swarm-over-Poker-2023* campaign (and perhaps also use convection flow data provided  
 496 by EISCAT 3D ([ref](#)) in the future). Additionally, the replication technique can pos-  
 497 sibly be merged with Lompe (Laundal et al., 2022) to provide even more self-consistency.

498 As a side note, a possible improvement to the replication technique would be to  
 499 have each individual plasma flow data point follow the conductance contour line it sits  
 500 on, while still rotating accordingly, creating essentially a continuous set of arc bound-  
 501 aries. This idea, however, has not yet been explored at the time of writing.

502 After gathering a sub-catalog of data driven simulations, they will be idealized to  
 503 retain only the simplest structures (peak precipitation flux, flow shear, arc width, etc.)  
 504 where the resulting data-*inspired* simulations can be defined by a manageable number  
 505 of parameters. From there, this parameter space will be strategically explored, gradu-  
 506 ally straying from their ideal, sheet-like structure, which will create the remainder of the  
 507 simulation catalog. From here, understanding the physical mechanisms connecting the  
 508 various parameters will aid in studying the data-driven simulations. This catalog and  
 509 its supplementary setup and driving infrastructure will be made publicly available in a  
 510 way that makes it easily expandable. This will all be covered in future paper, so stay  
 511 tuned.

512 **Open Research Section**

513 This section MUST contain a statement that describes where the data supporting  
 514 the conclusions can be obtained. Data cannot be listed as "Available from authors"  
 515 or stored solely in supporting information. Citations to archived data should be included  
 516 in your reference list. Wiley will publish it as a separate section on the paper's page. Ex-  
 517 amples and complete information are here: [https://www.agu.org/PublishwithAGU/  
 518 Publish/AuthorResources/Data for Authors](https://www.agu.org/PublishwithAGU/Publish/AuthorResources/DataforAuthors)

519 **Acknowledgments**

520 The Poker Flat Incoherent Scatter Radar is operated by the SRI International for the  
 521 National Science Foundation as part of the AMISR program through cooperative agree-  
 522 ment AGS-1840962. AMISR data are available at <https://data.amisr.com/database/>.  
 523 NSF CEDAR SoP2023, GEMINI grants, FINESST grant, NASA HEC if we use it, isin-  
 524 glass grant? arcs grant?, isinglass team: Meghan Burleigh, Robert Clayton, Guy Grubbs,  
 525 Donald L. Hampton, David Hysell, PH?, Robert Michell, Marilia Samara LL?

526 **References**

- 527 Ahlfors, L. V. (1953). Complex analysis: an introduction to the theory of analytic  
 528 functions of one complex variable. *New York, London, 177.*
- 529 Amm, O. (1997). Ionospheric elementary current systems in spherical coordinates  
 530 and their application. *Journal of geomagnetism and geoelectricity, 49(7), 947-*  
 531 *955.* doi: 10.5636/jgg.49.947
- 532 Bristow, W. A., Hampton, D. L., & Otto, A. (2016). High-spatial-resolution velocity  
 533 measurements derived using Local Divergence-Free Fitting of SuperDARN  
 534 observations. *Journal of Geophysical Research: Space Physics, 121(2), 1349-*  
 535 *1361.* Retrieved from <https://agupubs.onlinelibrary.wiley.com/doi/abs/10.1002/2015JA021862> doi: <https://doi.org/10.1002/2015JA021862>
- 537 Clayton, R., Burleigh, M., Lynch, K. A., Zettergren, M., Evans, T., Grubbs, G., ...  
 538 Varney, R. (2021). Examining the auroral ionosphere in three dimensions using  
 539 reconstructed 2D maps of auroral data to drive the 3D GEMINI model. *Jour-*  
 540 *nal of Geophysical Research: Space Physics, 126(11).* Retrieved from <https://agupubs.onlinelibrary.wiley.com/doi/abs/10.1029/2021JA029749> doi:  
 541 <https://doi.org/10.1029/2021JA029749>
- 543 Clayton, R., Lynch, K., Zettergren, M., Burleigh, M., Conde, M., Grubbs, G., ...  
 544 Varney, R. (2019). Two-dimensional maps of in situ ionospheric plasma  
 545 flow data near auroral arcs using auroral imagery. *Journal of Geophysi-*  
 546 *cal Research: Space Physics, 124(4), 3036-3056.* Retrieved from <https://agupubs.onlinelibrary.wiley.com/doi/abs/10.1029/2018JA026440> doi:  
 547 <https://doi.org/10.1029/2018JA026440>
- 549 Cowley, S. W. H. (2000). Magnetosphere-ionosphere interactions: A tutorial review.  
 550 *Magnetospheric Current Systems, Geophysical Monograph Series, 118, 91-106.*
- 551 Enengl, F., Kotova, D., Jin, Y., Clausen, L. B. N., & Miloch, W. J. (2023). Iono-  
 552 spheric plasma structuring in relation to auroral particle precipitation. *J.*  
 553 *Space Weather Space Clim., 13.* Retrieved from <https://doi.org/10.1051/swsc/2022038> doi: 10.1051/swsc/2022038
- 555 Erlandson, R., Lynch, K. A., Samara, M., Anderson, B., Bortnik, J., Burleigh, M., ...  
 556 Zou, S. (2024). *Auroral Reconstruction CubeSwarm (ARCS).* (Manuscript in  
 557 Preperation)
- 558 Fang, X., Randall, C. E., Lummerzheim, D., Solomon, S. C., Mills, M. J., Marsh,  
 559 D. R., ... Lu, G. (2008). Electron impact ionization: A new parameterization  
 560 for 100 ev to 1 mev electrons. *Journal of Geophysical Research: Space Physics,*  
 561 *113(A9).* Retrieved from <https://agupubs.onlinelibrary.wiley.com/doi/abs/10.1029/2008JA013384> doi: <https://doi.org/10.1029/2008JA013384>

- Fang, X., Randall, C. E., Lummerzheim, D., Wang, W., Lu, G., Solomon, S. C., & Frahm, R. A. (2010). Parameterization of monoenergetic electron impact ionization. *Geophysical Research Letters*, 37(22). Retrieved from <https://agupubs.onlinelibrary.wiley.com/doi/abs/10.1029/2010GL045406> doi: <https://doi.org/10.1029/2010GL045406>
- Fujii, R., Amm, O., Vanhamäki, H., Yoshikawa, A., & Ieda, A. (2012, 11). An application of the finite length cowling channel model to auroral arcs with longitudinal variations. *Journal of Geophysical Research*, 117. doi: [10.1029/2012JA017953](https://doi.org/10.1029/2012JA017953)
- Fujii, R., Amm, O., Yoshikawa, A., Ieda, A., & Vanhamäki, H. (2011). Reformulation and energy flow of the Cowling channel. *Journal of Geophysical Research: Space Physics*, 116(A2). Retrieved from <https://agupubs.onlinelibrary.wiley.com/doi/abs/10.1029/2010JA015989> doi: <https://doi.org/10.1029/2010JA015989>
- Heinselman, C. J., & Nicolls, M. J. (2008). A Bayesian approach to electric field and E-region neutral wind estimation with the Poker Flat Advanced Modular Incoherent Scatter Radar. *Radio Science*, 43(5). Retrieved from <https://agupubs.onlinelibrary.wiley.com/doi/abs/10.1029/2007RS003805> doi: <https://doi.org/10.1029/2007RS003805>
- Kamide, Y., Richmond, A. D., & Matsushita, S. (1981). Estimation of ionospheric electric fields, ionospheric currents, and field-aligned currents from ground magnetic records. *Journal of Geophysical Research: Space Physics*, 86(A2), 801-813. Retrieved from <https://agupubs.onlinelibrary.wiley.com/doi/abs/10.1029/JA086iA02p00801> doi: <https://doi.org/10.1029/JA086iA02p00801>
- Kelley, M. C. (2009). *The Earth's ionosphere: plasma physics and electrodynamics* (2nd ed.). Amsterdam, Netherlands: Academic Press.
- Kelly, J., & Heinselman, C. (2009). Initial results from Poker Flat Incoherent Scatter Radar (PFISR). *Journal of Atmospheric and Solar-Terrestrial Physics*, 71(6), 635. Retrieved from <https://www.sciencedirect.com/science/article/pii/S1364682609000121> (Advances in high latitude upper atmospheric science with the Poker Flat Incoherent Scatter Radar (PFISR)) doi: <https://doi.org/10.1016/j.jastp.2009.01.009>
- Khazanov, G. V., Robinson, R. M., Zesta, E., Sibeck, D. G., Chu, M., & Grubbs, G. A. (2018). Impact of precipitating electrons and magnetosphere-ionosphere coupling processes on ionospheric conductance. *Space Weather*, 16(7), 829-837. Retrieved from <https://agupubs.onlinelibrary.wiley.com/doi/abs/10.1029/2018SW001837> doi: <https://doi.org/10.1029/2018SW001837>
- Knudsen, D. J., Burchill, J. K., Buchert, S. C., Eriksson, A. I., Gill, R., Wahlund, J.-E., ... Moffat, B. (2017). Thermal ion imagers and langmuir probes in the Swarm electric field instruments. *Journal of Geophysical Research: Space Physics*, 122(2), 2655-2673. Retrieved from <https://agupubs.onlinelibrary.wiley.com/doi/abs/10.1002/2016JA022571> doi: <https://doi.org/10.1002/2016JA022571>
- Laundal, K. M., Reistad, J. P., Hatch, S. M., Madelaire, M., Walker, S., Hovland, A. Ø., ... Sorathia, K. A. (2022). Local mapping of polar ionospheric electrodynamics. *Journal of Geophysical Research: Space Physics*, 127(5). Retrieved from <https://agupubs.onlinelibrary.wiley.com/doi/abs/10.1029/2022JA030356> doi: <https://doi.org/10.1029/2022JA030356>
- Lotko, W. (2004). Inductive magnetosphere-ionosphere coupling. *Journal of Atmospheric and Solar-Terrestrial Physics*, 66(15), 1443-1456. Retrieved from <https://www.sciencedirect.com/science/article/pii/S1364682604001518> doi: <https://doi.org/10.1016/j.jastp.2004.03.027>
- Lynch, K. A., Erlandson, R., Samara, M., Anderson, B., Bortnik, J., Burleigh, M., ... Zou, S. (2024). *Auroral Reconstruction CubeSwarm (ARCS)*. (Manuscript in

- 618              Preperation)
- 619    Lynch, K. A., McManus, E., Gutow, J., Burleigh, M., & Zettergren, M. (2022). An  
620          ionospheric conductance gradient driver for subauroral picket fence visible sig-  
621          natures near STEVE events. *Journal of Geophysical Research: Space Physics*,  
622          127(12). Retrieved from <https://agupubs.onlinelibrary.wiley.com/doi/abs/10.1029/2022JA030863> doi: <https://doi.org/10.1029/2022JA030863>
- 623    Mallinckrodt, A. J. (1985). A numerical simulation of auroral ionospheric electro-  
624          dynamics. *Journal of Geophysical Research: Space Physics*, 90(A1), 409-417.  
625          Retrieved from <https://agupubs.onlinelibrary.wiley.com/doi/abs/10.1029/JA090iA01p00409> doi: <https://doi.org/10.1029/JA090iA01p00409>
- 626    Marghitu, O. (2012). Auroral arc electrodynamics: Review and outlook. *Rela-  
627          tionship between auroral phenomenology and magnetospheric processes: Earth and  
628          other planets, Geophysical Monograph Series*, 197, 143-158.
- 629    Mule, A. (2023, October 1). Personal communication.
- 630    Mule, A. (2024, February 8). Personal communication.
- 631    Nicolls, M. J., Cosgrove, R., & Bahcivan, H. (2014). Estimating the vector  
632          electric field using monostatic, multibeam incoherent scatter radar mea-  
633          surements. *Radio Science*, 49(11), 1124-1139. Retrieved from <https://agupubs.onlinelibrary.wiley.com/doi/abs/10.1002/2014RS005519> doi:  
634          <https://doi.org/10.1002/2014RS005519>
- 635    Nicolls, M. J., & Heinselman, C. J. (2007). Three-dimensional measurements  
636          of traveling ionospheric disturbances with the Poker Flat Incoherent Scat-  
637          ter Radar. *Geophysical Research Letters*, 34(21). Retrieved from <https://agupubs.onlinelibrary.wiley.com/doi/abs/10.1029/2007GL031506> doi:  
638          <https://doi.org/10.1029/2007GL031506>
- 639    Richmond, A. D., & Kamide, Y. (1988). Mapping electrodynamic features of  
640          the high-latitude ionosphere from localized observations: Technique. *Jour-  
641          nal of Geophysical Research: Space Physics*, 93(A6), 5741-5759. Retrieved  
642          from <https://agupubs.onlinelibrary.wiley.com/doi/abs/10.1029/JA093iA06p05741> doi: <https://doi.org/10.1029/JA093iA06p05741>
- 643    Robinson, R. M., Vondrak, R. R., Miller, K., Dabbs, T., & Hardy, D. (1987). On  
644          calculating ionospheric conductances from the flux and energy of precipitating  
645          electrons. *Journal of Geophysical Research: Space Physics*, 92(A3), 2565-  
646          2569. Retrieved from <https://agupubs.onlinelibrary.wiley.com/doi/abs/10.1029/JA092iA03p02565> doi: <https://doi.org/10.1029/JA092iA03p02565>
- 647    Ruohoniemi, J. M., Greenwald, R. A., Baker, K. B., Villain, J. P., Hanuise, C., &  
648          Kelly, J. (1989). Mapping high-latitude plasma convection with coherent HF  
649          radars. *Journal of Geophysical Research: Space Physics*, 94(A10), 13463-13477.  
650          Retrieved from <https://agupubs.onlinelibrary.wiley.com/doi/abs/10.1029/JA094iA10p13463> doi: <https://doi.org/10.1029/JA094iA10p13463>
- 651    Seyler, C. E. (1990). A mathematical model of the structure and evolu-  
652          tion of small-scale discrete auroral arcs. *Journal of Geophysical Re-  
653          search: Space Physics*, 95(A10), 17199-17215. Retrieved from <https://agupubs.onlinelibrary.wiley.com/doi/abs/10.1029/JA095iA10p17199>  
654          doi: <https://doi.org/10.1029/JA095iA10p17199>
- 655    Sobel, I. (2014, 02). An isotropic 3x3 image gradient operator. *Presentation at Stan-  
656          ford A.I. Project 1968*.
- 657    Solomon, S. C. (2017). Global modeling of thermospheric airglow in the far ultra-  
658          violet. *Journal of Geophysical Research: Space Physics*, 122(7), 7834-7848.  
659          Retrieved from <https://agupubs.onlinelibrary.wiley.com/doi/abs/10.1002/2017JA024314> doi: <https://doi.org/10.1002/2017JA024314>
- 660    Wang, X., Cai, L., Aikio, A., Vanhamäki, H., Virtanen, I., Zhang, Y., ... Liu,  
661          S. (2024). Ionospheric conductances due to electron and ion precipita-  
662          tions: A comparison between EISCAT and DMSP estimates. *Journal of  
663          Geophysical Research: Space Physics*, 129(2). Retrieved from <https://agupubs.onlinelibrary.wiley.com/doi/abs/10.1029/JA095iA10p17199>
- 664          doi: <https://doi.org/10.1029/JA095iA10p17199>

- 673 agupubs.onlinelibrary.wiley.com/doi/abs/10.1029/2023JA032354 doi:  
674 https://doi.org/10.1029/2023JA032354

675 Wolf, R. A. (1975, Mar 01). Ionosphere-magnetosphere coupling. *Space Science Re-*  
676 *views*, 17(2), 537-562. Retrieved from <https://doi.org/10.1007/BF00718584>  
677 doi: 10.1007/BF00718584

678 Yano, Y., & Ebihara, Y. (2021). Three-dimensional closure of field-aligned cur-  
679 rents in the polar ionosphere. *Journal of Geophysical Research: Space Physics*,  
680 126(9). Retrieved from <https://agupubs.onlinelibrary.wiley.com/doi/abs/10.1029/2021JA029421> doi: <https://doi.org/10.1029/2021JA029421>

681 Zettergren, M., & Snively, J. (2019). Latitude and longitude dependence of iono-  
682 spheric TEC and magnetic perturbations from infrasonic-acoustic waves gener-  
683 ated by strong seismic events. *Geophysical Research Letters*, 46(3), 1132-1140.  
684 doi: 10.1029/2018GL081569

685 Zettergren, M. D., & Semeter, J. L. (2012). Ionospheric plasma transport and  
686 loss in auroral downward current regions. *Journal of Geophysical Research: Space  
687 Physics*, 117(A6). Retrieved from <https://agupubs.onlinelibrary.wiley.com/doi/abs/10.1029/2012JA017637> doi: <https://doi.org/10.1029/2012JA017637>

688

689

690